

Citation for published version: Williamson, D, Jones, M & Mattia, D 2019, 'Highly selective, iron-driven CO2 methanation', *Energy Technology*, vol. 7, no. 2, pp. 294-306. https://doi.org/10.1002/ente.201800923

DOI:

10.1002/ente.201800923

Publication date: 2019

Document Version Peer reviewed version

Link to publication

This is the peer-reviewed version of the following article: Williamson, D, Jones, M & Mattia, D 2018, 'Highly selective, iron-driven CO2 methanation Energy Technology. which has been published in final form at: https://doi.org/10.1002/ente.201800923. This article may be used for non-commercial purposes in accordance with Wiley Terms and conditions for Self-Archiving.

## **University of Bath**

## **Alternative formats**

If you require this document in an alternative format, please contact: openaccess@bath.ac.uk

Copyright and moral rights for the publications made accessible in the public portal are retained by the authors and/or other copyright owners and it is a condition of accessing publications that users recognise and abide by the legal requirements associated with these rights.

**Take down policy**If you believe that this document breaches copyright please contact us providing details, and we will remove access to the work immediately and investigate your claim.

Download date: 09 Mar 2023

# Highly selective, iron-driven CO<sub>2</sub> methanation

David L. Williamson, [a] Matthew D. Jones\*[b] and Davide Mattia\*[a]

Abstract: CO<sub>2</sub> methanation has gained traction for its potential in renewable energy storage, though the high cost of renewable hydrogen production and costly metals used in methanation catalyst synthesis remain a significant barrier to implementation. Herein we present a Ru-Fe@NCNT catalyst, consisting of ruthenium and iron nanoparticles on nitrogen-doped carbon nanotubes, as a highly selective, hydrogen efficient, iron-driven alternative to typical nickel and ruthenium catalysts used for CO and CO<sub>2</sub> methanation. Ru-Fe@NCNT offer competitive CO<sub>2</sub> conversion and methane selectivity, and a reduction of up to 80% in ruthenium loading versus similar literature and commercial catalysts. It is proposed that this desirable CO<sub>2</sub> methanation performance is a result of effective cooperation between the iron-catalysed reverse water gas shift and methane-selective Fischer-Tropsch, and ruthenium-catalysed CO methanation reactions.

#### Introduction

CO and CO<sub>2</sub> methanation have long been used in industry, typically to produce synthetic natural gas or to avoid catalyst poisoning in ammonia production.[1] In recent years these processes have garnered additional interest as a means of storing excess wind and solar energy as methane in existing natural gas grids due to their large potential storage capacity, by coupling waste CO2 with renewable hydrogen as reagents. While this application is potentially valuable, the high cost of renewable hydrogen production and scarcity of high purity CO2 streams have prohibited large scale implementation of such technologies.[2] However, advances in the efficiency of water electrolysis processes are anticipated to reach a point of commercial viability in the coming years, supporting the need for concurrent research on active, selective and cost-effective CO<sub>2</sub> methanation catalysts to make the overall process of CO2 methanation for energy storage as effective as possible. [2b, 2d]

Ruthenium, nickel and iron have been identified as the most active species for CO methanation, with nickel being the preferred choice in industry owing to its favourable balance between activity, selectivity and cost. Ruthenium and iron are recognized as having higher activity than nickel but are less suitable for industry due to the high cost of ruthenium and the tendency towards side reactions observed in iron-based catalysts despite it being the least expensive of these metals.<sup>[3]</sup> Ranking metal activity in CO<sub>2</sub>

[a] David L. Williamson, Dr Davide Mattia Department of Chemical Engineering University of Bath Claverton Down, Bath BA2 7AY (UK) E-mail: d.mattia@bath.ac.uk

[b] Dr Matthew D. Jones
Department of Chemistry
University of Bath
Claverton Down, Bath BA2 7AY (UK)
E-mail: m.jones2@bath.ac.uk

Supporting information for this article is given via a link at the end of the document.

methanation has proven to be a more complex undertaking. While typical CO methanation catalysts also display high activity in CO2 methanation, their activities suffer notably when methanising CO<sub>2</sub> rather than CO due to its enhanced thermodynamic stability. It has been noted that the activity and selectivity of iron-based catalysts suffer in particular when applied in CO<sub>2</sub> methanation. [3c, 4] This has been previously attributed to "overbinding" of CO2 on Fe causing a thermodynamic sink on the reaction coordinate. [5] However, it must be noted that the mechanism of CO<sub>2</sub> methanation remains poorly understood, with current discussion in literature centring around the possible associative versus dissociative pathways to direct CO<sub>2</sub> methanation. [6] While iron appears to suffer in activity towards direct CO2 methanation relative to other active CO methanation catalysts, it remains a highly active water-gas shift catalyst, allowing for the reduction of CO2 to CO, and a preferred Fischer-Tropsch (FT) catalyst, allowing for the production of varied hydrocarbons and alcohols from CO. Thus, an alternate pathway to methane production from CO2 over iron-based catalysts exists, which relies on effective coupling of these two reactions rather than relying on the direct CO2 methanation pathway.

Common industrial methanation catalysts operate via the Sabatier reaction (Equation 1), which is assumed to proceed through one of the proposed direct  $CO_2$  methanation mechanisms, and are thus operated using a feed gas where at  $P_{H2}/P_{CO2} = 4$ . [7]

$$CO_2 + 4H_2 \rightleftharpoons CH_4 + 2H_2O$$
 (1)

Parallel to CO<sub>2</sub> methanation, significant research has also been invested in coupling Reverse Water-Gas Shift (RWGS) and FT chemistry to produce longer chain hydrocarbons beyond CH<sub>4</sub>. In combined RWGS/FT chemistry, CO<sub>2</sub> is initially reduced to CO via RWGS (Equation 2), and the resulting CO is then consumed in FT to produce a distribution of hydrocarbon species (Equation 4):<sup>[8]</sup>

$$CO_2 + H_2 \rightleftharpoons CO + H_2O \tag{2}$$

$$nCO + (2n+1)H_2 \rightarrow C_nH_{2n+2} + nH_2O$$
 (3)

Iron species are known to catalyse both of these reactions, [8b] and it has been shown that combining the RWGS reaction with the irreversible FT process shifts the equilibrium of the RWGS reaction towards products, making both reactions favourable under similar conditions and improving the efficiency of the overall CO<sub>2</sub> hydrogenation process relative to performing the two reactions separately. [9] While methane is a common product of combined RWGS/FT processes, the additional hydrocarbon species produced (e.g. olefins and higher hydrocarbons) have been the primary targets for research thus far, and have left RWGS/FT chemistry under explored as a route to selective methanation. A notable difference between combined RWGS/FT and Sabatier chemistry is that the ideal value of PH2/PCO2 for combined RWGS/FT processes has been consistently cited in literature as 3 rather than the standard value of 4 for direct CO<sub>2</sub> methanation.[8b, 10] This reflects the multi-reaction mechanism involved in combined RWGS/FT processes, and it has been previously claimed that starving the process of hydrogen in such a manner encourages the formation of higher hydrocarbon products. [10a] However, it remains unclear whether  $P_{H2}/P_{CO2} = 4$  would thus be preferable when targeting methane as a product. While this difference in feed composition does not provide any inherent advantages over traditional methanation processes, it does suggest an alternate mechanism to methanation that proceeds preferentially over iron-based catalysts, which may offer cost saving opportunities without notable drawbacks in our efforts to develop effective  $CO_2$  methanation processes for renewable energy storage.

Previous studies have outlined the activity of iron-decorated carbon nanotube catalysts (Fe@CNT) in combined RWGS/FT catalysis.[11] The catalysts are produced via a single-step CVD synthesis technique in which iron nanoparticles nucleate the growth of the carbon nanotube (CNT) support, thereby becoming embedded on the CNT wall structure directly during synthesis. The same iron particles that nucleate the CNT growth are then able to act as catalytic sites for combined RWGS/FT chemistry. displaying superior activity to similar materials where the iron particles are doped onto the surface via wet impregnation due to increased interaction between the catalytic iron and the CNT support.[11a] This single-step approach thus produces an appealing CO<sub>2</sub> hydrogenation catalyst due to its high activity and reduced complexity of manufacturing. [11c] As expected for ironcatalysed RWGS/FT processes, the product distributions are reported as a mixture of primarily carbon monoxide and C1-C4 hydrocarbons, with initial research efforts focused on shifting the product distribution towards higher hydrocarbons and olefinparaffin ratios through manipulation of the reaction conditions and addition of promoters.

Herein we present the Ru-Fe@NCNT material as a ruthenium-and nitrogen-doped, iron-driven CO<sub>2</sub> methanation catalyst with high activity, selectivity, and hydrogen efficiency. The material is analogous to the aforementioned Fe@CNT, where nitrogen has been incorporated directly into the catalyst support during CVD synthesis, and ruthenium has been doped onto the surface via a conventional wet impregnation technique. Ru-Fe@NCNT display highly competitive CO<sub>2</sub> methanation performance and hydrogen utilisation while reducing the ruthenium loading requirement by ca. 66-80% compared to literature catalysts, and confirming an ideal value of  $P_{H2}/P_{CO2}$  = 3, even when targeting methane as a product in combined RWGS/FT chemistry.

## **Results and Discussion**

#### **Catalyst characterization**

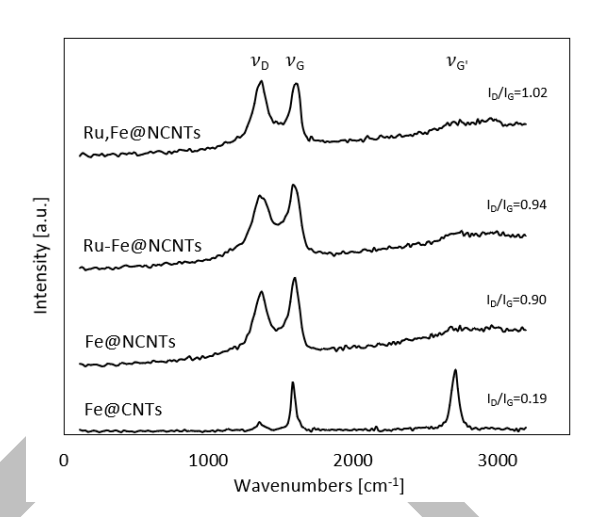


**Figure 1.** Raman spectra of Fe@CNT, Fe@NCNT, Ru-Fe@NCNT, and Ru,Fe@NCNT-0.2/1.0 activated at 400 °C in air for 1 hour.

To confirm the successful synthesis of Fe@NCNT, Ru-Fe@NCNT and Ru,Fe@NCNT, all materials were analysed via Raman, SEM, TEM, and XPS. In the Raman analysis, pristine Fe@CNT (with neither ruthenium nor nitrogen doping) have been included for reference purposes.

Raman analysis of all three activated materials displayed clear peaks at 1354 cm<sup>-1</sup> and 1597 cm<sup>-1</sup> (Fig. 1). These are referred to as the D and G bands, respectively, and are commonly observed in the Raman spectra of CNT-derived materials. The D peak becomes more pronounced as the number of lattice defects in the sample increases, and so the ratio of the D and G peaks (ID/IG) is used as a measure of the overall order in a sample.[12] As expected, the reference Fe@CNT displayed a low ID/IG value of 0.19, while values of 0.90, 0.94 and 1.02 were obtained for Fe@NCNT, Ru-Fe@NCNT, and Ru,Fe@NCNT, respectively. This confirms progressively increasing disorder in these materials due to the addition of nitrogen and ruthenium.[13] Nitrogen incorporation increases the disorder of all NCNT-based samples due to lattice defects that evolve as a result of nitrogen's inability to fully assimilate into the sp<sup>2</sup> hybridized CNT lattice as well as the carbon it replaces.[14] Post-doping of ruthenium via incipient wetness may damage the NCNT supports slightly through prolonged stirring and heating to remove the solvent. CVD doping results in the greatest increase in defects. This is expected as, unlike ferrocene, ruthenocene is not known to nucleate CNT growth. Thus, its incorporation likely results in some inhibition of the ordered ferrocene-based CNT growth mechanism. An additional feature is observed in the spectra of all three materials at ca. 2666 cm<sup>-1</sup> and 2977 cm<sup>-1</sup>. These broad, low intensity peaks may be attributed to the suppressed 2D band (also known as the G' band), which is indicative of long-range order in a sample. [15] This band is often noted to be sharp and clear in pristine CNT materials such as the Fe@CNT, where it is clearly visible, but becomes suppressed in NCNTs due to the introduction of the same lattice defects that result in the increase of the D peak.

XPS analysis was used to determine the effect of activation and catalytic application on the elemental composition of the catalysts (all values reported in SI Table 1). Fe@NCNT appear to be composed of nitrogen, oxygen and a small amount of iron directly after synthesis. Upon thermal activation to expose the catalytic iron particles, nitrogen content decreases while oxygen and iron increases. The decrease in nitrogen is attributed to the release of physisorbed molecular N2 and chemisorbed N-O species at the surface,[13-14, 16] while the increase in oxygen is attributed to formation of new C-O and iron oxide species as a result of the oxidation process; this is supported by a decrease in the N-O peak in the N 1s region and increases in the iron oxidation state in the Fe 2p region, as discussed below. The increase in iron is due to the removal of a graphitic carbon layer concealing the Fe nanoparticles initially after synthesis, thus exposing them for catalysis.[11a] After reaction, the concentrations of all three elements decreased notably. The decrease in nitrogen suggests that either the reduction step or the methanation process may be capable of breaking some C-N bonds in the NCNT support structure, reducing the nitrogen content of the catalyst. The significant decrease in oxygen is expected, as the reduction and reaction steps serve to significantly reduce the metal oxides formed during the highly oxidizing activation process. The decrease in iron is attributed to carbon deposition onto the iron particles during the reaction process. Carbon deposition also likely contributes to the observed decrease in nitrogen and oxygen due to a relative increase in carbon content.

XPS of post-doped Ru-Fe@NCNT indicates the presence of iron, nitrogen and ruthenium after the activation step. The ruthenium mass loading is calculated to be 1.6 wt. % from the atom % concentration measured during XPS, which is in good agreement with the 1.0 wt. % mass loading targeted during catalyst synthesis. Surface iron loading was similarly determined to be 3.5 wt. %. After reaction, the iron, nitrogen and ruthenium concentrations also decrease. This is consistent with the decrease in nitrogen and iron observed in standard Fe@NCNT, and may be similarly attributed to the removal of nitrogen during the reduction or reaction steps, and carbon deposition during the reaction resulting in a lower observed concentration of other elements in the sample. These repeated trends in Ru-Fe@NCNT and Fe@NCNT suggest that the incipient wetness ruthenium doping process has little effect on the chemical composition of the underlying Fe@NCNT beyond the desired ruthenium addition.

CVD-doped Ru,Fe@NCNT follows several of the same trends observed in Fe@NCNT and post-doped Ru-Fe@NCNT. The elemental concentrations of iron, nitrogen and ruthenium are similar in the fresh and activated samples, and again the nitrogen content decreases upon activation, while the iron, oxygen and ruthenium concentrations increase. After reaction, the oxygen,

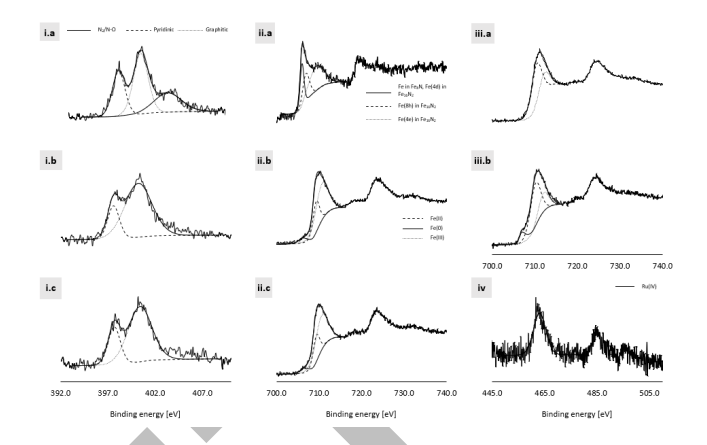


**Figure 2.** XPS spectra of (i) Fe@NCNT N 1s region (ii) Fe@NCNT and Ru-Fe@NCNT Fe 2p region, (a) freshly synthesized, (b) activated at 400 °C in air for 1 hour, and (c) after a typical CO<sub>2</sub> methanation reaction. (iii) Ru,Fe@NCNT Fe 2p region, (a) activated at 400 °C in air for 1 hour, and (b) after a typical methanation reaction. (iv) Ru-Fe@NCNT Ru 3p region activated at 400 °C in air for 1 hour.

iron and ruthenium content are observed to decrease, similarly to Fe@NCNT and Ru-Fe@NCNT. However, it is noteworthy that the nitrogen content increases rather than decreased, as was observed in all other samples. This could be due to more efficient incorporation of the nitrogen during synthesis as a result of the CVD-doped ruthenium, or it may be due to the different reactivity of this material, as the CVD-doped Ru,Fe@NCNT are later noted to have lower conversion and greater selectivity towards long-chain hydrocarbons than the post-doped Ru-Fe@NCNT.

N 1s regions of the catalysts reveal similar compositions and trends across all samples. Immediately after CVD synthesis, the N 1s region is de-convoluted to display peaks at ca. 398.8, 401.3, and 404.4 eV (Fig. 2[i.a]), which are attributed to pyridinic, graphitic, and physisorbed molecular N2 or chemisorbed N-O species, respectively.[13-14, 16a, 16b] The ratios of these peak areas are typically on the order of 1:2:1, suggesting that graphitic nitrogen is the primary species incorporated in the NCNT lattice during synthesis. Literature studies of similar NCNTs have also reported a peak at ca. 400.0 eV as a result of pyrrolic nitrogen, though this peak does not appear in any of the materials discussed here. Following activation, the peaks for graphitic and pyridinic nitrogen remain, with peak area ratios of ca. 3:1, suggesting that the tubes consist largely of graphitic-bound nitrogen prior to methanation testing (Fig. 2[i.b]). The N-O peak is significantly suppressed after activation, suggesting the removal of the aforementioned molecular N2 and N-O bound nitrogen via oxidation. No notable changes in the nitrogen species were observed in the catalysts following reaction (Fig. 2[i.c]).

Fe 2p regions of the catalysts reveal a notable difference between the iron species present in post-doped Ru-Fe@NCNT and CVD-doped Ru,Fe@NCNT (Fig. 2[ii.a-iii.b]). Directly after synthesis, Fe@NCNT, Ru-Fe@NCNT, and Ru,Fe@NCNT all exhibit peaks at 707.2, 708.0, and 710.5 eV, which are attributed to the iron nitride species Fe<sub>8</sub>N and Fe<sub>16</sub>N<sub>2</sub> (Fig. 2[i.a]).<sup>[17]</sup> After activation

these peaks shift to 707.5, 709.9, and 711.3 eV, which are attributed to Fe(0), Fe(II) and Fe(III), respectively (Fig. 2[ii.b, iii.a]).[18] These peaks suggest a change in the iron species from nitrides to a mix of Fe<sub>2</sub>O<sub>3</sub> and Fe<sub>3</sub>O<sub>4</sub> as the iron particles are exposed from underneath the graphitic layer of carbon and nitrogen, and transformed into iron oxide. This corresponds with the increase in iron and oxygen concentrations observed after activation (SI Table 1). In Fe@NCNT and Ru-Fe@NCNT, identical iron trends are observed with Fe(III) being the dominant species, suggesting a significant concentration of Fe<sub>2</sub>O<sub>3</sub> that is confirmed by the presence of a slight satellite peak at ca. 718.8 eV. The small Fe(0) shoulder is attributed to iron that was partially exposed by the activation process but remains unoxidized (Fig. 2[ii.b]).[11a] No notable is was observed in Fe@NCNT and Ru-Fe@NCNT after methanation testing (Fig. 2[ii.c]). Ru,Fe@NCNT, Fe(II) is noted to be the dominant species after activation and methanation testing, with a small Fe(0) shoulder appearing after methanation (Fig. 2[iii.b]). This suggests that the inclusion of ruthenium during the CVD synthesis process serves to inhibit the oxidation of the iron, either by favouring the formation of Fe<sub>3</sub>O<sub>4</sub> or through a more complex electronic interactions between the iron and ruthenium. To the authors' knowledge this is the first known example of co-doping bimetallic nanoparticles directly onto carbon nanotube supports via CVD. As such, the precise relationship between the two metals in this doping configuration remains unclear. However, the mirrored Fe 2p spectra between Fe@NCNT and Ru-Fe@NCNT suggest that the iron remains unchanged by the incipient wetness ruthenium doping process, implying that the iron in Ru-Fe@NCNT is likely to behave similarly to the iron in Fe@NCNT during catalysis. Similarly, the differences in iron oxidation states between Ru-Fe@NCNT and Ru,Fe@NCNT serve as a plausible explanation for any observed differences in reactivity between them.

Ru 3p regions of the catalysts suggest the possible presence of metallic ruthenium, ruthenium carbide and ruthenium oxide, with some deviation from standard peak positions (Fig. 2[iv]). Due to strong overlap between the Ru 3d and C 1s regions of the XPS spectra, the Ru 3p 3/2 region was used instead to determine the composition of the doped ruthenium. In all samples, a single peak is observed. In post-doped Ru-Fe@NCNT, the peak is observed at 463.1 eV after activation, shifting to 462.7 eV after reaction. This trend is reflected in activated and post-reaction Ru,Fe@NCNT as well, with the observed peak shifting from 463.0 eV to 461.5 eV in the Ru,Fe@NCNT-0.05/0.95 sample, and from 463.1 eV to 462.1 eV in the Ru,Fe@NCNT-0.2/1.0 sample. Ru(0) has a characteristic peak at ca. 461.2 eV, while RuO2 has characteristic peaks at 462.6 eV and 464.0 eV.[18b, 19] No ruthenium species has been identified with a characteristic peak at 463.1 eV, so this peak shift has been tentatively assigned as either a shift from RuO2 after activation to Ru(0) after reaction, or merely a shift in the RuO2 peak with no change in oxidation state. [19b] In fresh Ru, Fe@NCNT the peak is observed at 459.2 eV in the Ru,Fe@NCNT-0.05/0.95 sample, and at 461.8 eV in the Ru,Fe@NCNT-0.2/1.0 sample. These peaks are both attributed to either Ru(0) or Ru carbide, [19b] as the CVD-doped ruthenium is likely incorporated directly into the NCNT support structure,

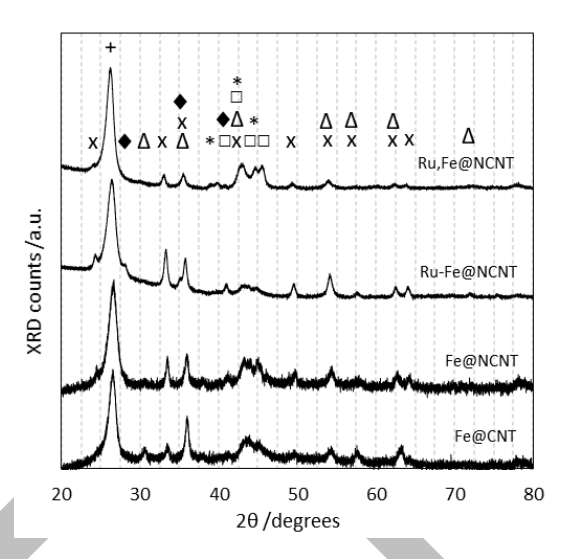


Figure 3. XRD spectra of Fe@CNT, Fe@NCNT, Ru-Fe@NCNT and Ru,Fe@NCNT-0.2/1.0 after activation at 400 °C (or 570 °C for Fe@CNT) in air for 1 hour. The spectra indicate the presence of the CNT support (+), Fe $_2$ O $_3$  (x), Fe $_3$ O $_4$  ( $\triangle$ ), iron carbides ( $\blacksquare$ ), metallic Ru (\*), and RuO $_2$  ( $\blacklozenge$ ).

similar to the Fe nanoparticles. In the absence of characteristic peak positions, these assignments are justified by the oxygen-free CVD synthesis environment, in which the formation of Ru oxides in the fresh samples is significantly less likely than the formation of Ru(0) or Ru carbides as the particles are formed and similarly covered with a graphitic carbon layer.

pXRD was used to further confirm catalyst composition and phase, specifically with respect to identifying the formation of composites or alloys of the iron and ruthenium, which might influence catalytic performance due to electronic interactions between the two metals (Fig. 3). XRD spectra all displayed an intense reflection at 26.4°, which is attributed to the CNT support. Samples also displayed peaks at 30.5°, 35.8°, 43.4°, 54.1°, 57.6°, and 62.5° for Fe<sub>3</sub>O<sub>4</sub>,<sup>[20]</sup> and 24.2°, 30.4, 33.3°, 35.8°, 41.0°, 49.6°, 54.1°, 57.6°, 62.5°, and 63.9° for Fe<sub>2</sub>O<sub>3</sub>.[21] Iron carbides were visible in all samples even after activation in air as a characteristic grouping of overlapping peaks between 20 values of 40° and 50°.[22] Ruthenium was visible in both Ru-Fe@NCNT and Ru,Fe@NCNT-0.2/1.0 in the form of metallic ruthenium with peaks at 38.9°, 43.0°, and 44.6°, though the latter peaks are largely obscured by the presence of iron carbides in the sample. RuO2 was additionally detected, with peaks at 20 values of 28.0°, 35.1°, and 41.0°. [23]

It is noteworthy that Fe@CNT display more intense peaks for the observed iron oxides when compared with Fe@CNT, though this is likely due to the higher oxidation temperature used when activating the Fe@CNT. It is additionally noteworthy that while the peaks for all ruthenium species are of a relatively low intensity, which is expected due to the small amount of ruthenium used, the ruthenium species observed in Ru-Fe@NCNT and Ru,Fe@NCNT are distinctly different. Ru-Fe@NCNT shows the clear presence of RuO<sub>2</sub> in small shoulder peaks at 28.0° and 35.1° with no clear contribution from metallic ruthenium, while

Ru,Fe@NCNT shows a clear contribution from metallic ruthenium at 38.9° with no clear contribution from RuO2. Ru,Fe@NCNT display a less intense contribution from the iron oxide species and a stronger contribution from the iron carbides between the two ruthenium-doped materials, while the opposite trend is observed in Ru-Fe@NCNT. Some caution must be applied in attributing significance to the intensity of these peaks, as their intensities rely significantly upon particle size and crystallinity – factors which remain unexplored at this time – in addition to the relative concentration of each species in the sample.

However, it may also be significant that Ru,Fe@NCNT appear to stabilize iron carbides and lower oxidation states of iron, a trend that is agreement with XPS analysis (Fig. 2), as the Hägg carbide (cementite) is known to be the active phase in iron-drive FT catalysis.<sup>[24]</sup> A catalyst that stabilizes more reduced forms of iron and allows for more facile formation of the Hägg carbide during catalysis would be expected to have high activity in the FT reaction and good capability for chain lengthening to higher hydrocarbon products: a trend that is observed in the product distribution of Ru.Fe@NCNT versus Ru-Fe@NCNT (Fig. 7). Thus. while the pXRD spectra of Ru-Fe@NCNT and Ru,Fe@NCNT cannot definitively confirm or exclude the formation of ironruthenium composites or alloys in either catalyst, the different ruthenium species observed in each catalyst may suggest greater electronic interactions between the iron and ruthenium in Ru,Fe@NCNT versus Ru-Fe@NCNT where they appear to be largely independent - a relationship that is supported by XPS analysis and their significantly different product distributions.

FESEM analysis of post-doped Ru-Fe@NCNT showed the underlying Fe@NCNT bundles in good condition subsequent to the incipient wetness doping process (Fig. 4[i]). The bundles maintained their highly-aligned, tight-packed growth pattern, suggesting that the doping process does not notably disperse the tubes or alter their orientation on the microscale. SEM analysis of the CVD-doped Ru,Fe@NCNT shows the clear formation of tube bundles, similar to those formed in standard Fe@NCNT CVD

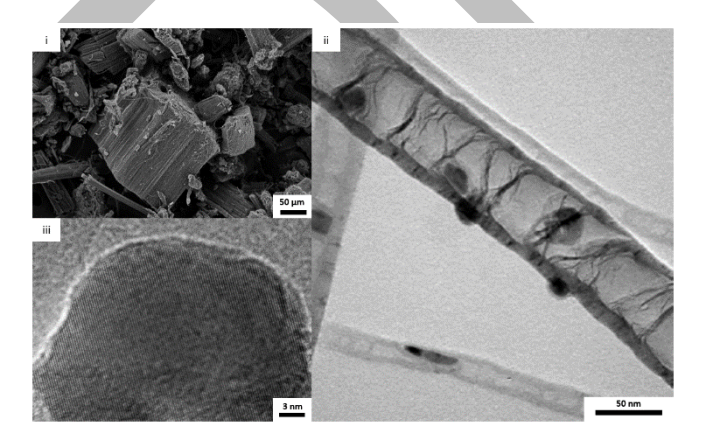


**Figure 4.** (i) FESEM micrograph of Ru-Fe@NCNT directly after incipient wetness doping. (ii) TEM micrograph of Ru-Fe@NCNT after activation at 400 °C in air for 1 hour. (iii) TEM micrograph depicting the crystal lattice of a single supported iron oxide particle after activation at 400 °C in air for 1 hour.

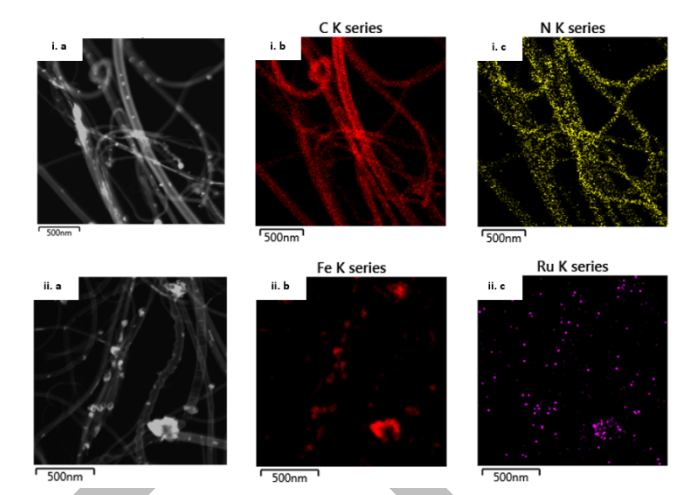


**Figure 5.** EDX maps of Ru-Fe@NCNT after activation at 400 °C in air for 1 hour. Nitrogen is visibly dispersed throughout the support structure in Ru-Fe@NCNT (i.c), which was reflected in Ru,Fe@NCNT as well (not shown). In Ru-Fe@NCNT, ruthenium appears scattered along the catalyst (ii.c), while in Ru,Fe@NCNT ruthenium appears exclusively localized within iron particles, though not all iron particles appear to contain ruthenium (SI Fig. 4[iii.a-c]).

synthesis (SI Fig. 1). While the Ru,Fe@NCNT-0.05/0.95 sample displayed highly aligned bundles that were indistinguishable from Fe@NCNT, the Ru,Fe@NCNT-0.2/1.0 sample displayed tube bundles growing in a semi-spherical, orange-peel-like orientation which is attributed to the greater ruthenocene loading employed during synthesis (SI Fig. 1[iii-iv]). This is a significant deviation from the tightly packed, linearly aligned bundles observed in typical Fe@CNT and Fe@NCNT, and indicates that the addition of ruthenocene does affect the CNT growth mechanism during synthesis, as initially suggested by the increase in I<sub>D</sub>/I<sub>G</sub> observed in the Raman spectrum.

TEM analysis of post-doped Ru-Fe@NCNT clearly depicts tubes with diameters of 20-100 nm and iron particles with diameters of 20-50 nm embedded in the tube walls (Fig. 4[ii, iii]). This is consistent with previous TEM analysis of the Fe@CNT catalyst.[11a] The lateral texturing along the tube walls is sometimes referred to as bamboo segmentation, and is a common indication of successful nitrogen doping into the CNT support during the CVD synthesis process. The effect is caused by lattice defects that result in deviations from the ordered growth pattern observed in pristine CNTs, as nitrogen cannot be incorporated into the sp2 hybridized CNT lattice as easily as carbon.<sup>[25]</sup> EDX maps confirm the presence of nitrogen along the tube support structure (Fig. 5[i.c]), as well as iron in localized particles on both the interior and exterior of the NCNT tube support (Fig. 5[ii.b]). Ruthenium appears to be lightly dispersed along the tubes (Fig. 5[ii.c]). In some instances, ruthenium particles of ca. 2-5 nm appeared to agglomerate onto the surface of larger iron particles, though no more intimate integration of the iron and ruthenium is observed (Fig. 5[ii.c]). This is in agreement with the lack of change in the iron species observed in the XPS (Fig. 2[ii.a-c]) after incipient wetness ruthenium doping, which

would be an expected result of electronic interactions between iron and ruthenium arising from alloy or composite formation.

CVD-doped Ru,Fe@NCNT samples clearly display the presence of tubes with similar dimensions to the Ru-Fe@NCNT (SI Fig. 2). Iron particles remain embedded in the tube walls and wall texturing indicative of nitrogen doping remained visible. EDX maps again confirm the presence of localized iron particles supported on the tube walls as well as larger metal slugs filling the inner tube cavity, as observed in Fe@NCNT and Ru-Fe@NCNT (Fig. 5[ii.a-b]). However, ruthenium appears to be more intimately integrated into the iron particles as a result of the CVD doping process (SI Fig. 4[iiii.b-c]). While pure iron oxide particles are clearly visible and abundant in the sample, ruthenium is not observed unless it is part of an existing iron particle. Closer examination of the iron-ruthenium particles reveals several distinct lattice orientations overlapping in each particle rather than a single crystalline phase, as would be observed in a pure iron oxide particle (SI Fig. 3). This suggests that the CVD doping process results in iron-ruthenium composite particles, which is supported by the difference in iron oxidation state observed via XPS, the difference in ruthenium species and apparent increase in iron carbide species observed between the XRD spectra of Ru-Fe@NCNT and Ru,Fe@NCNT, and the deviation in growth orientation observed via SEM (SI Fig. 1), as the ruthenium may be interfering with the active phase of the iron particles during arowth.[26]

#### CO<sub>2</sub> methanation performance

Fe@CNT (without nitrogen or ruthenium) were used as a baseline reference material during testing and resulted in 48% CO<sub>2</sub> conversion, producing a range of C<sub>1</sub>-C<sub>4</sub> hydrocarbons with an olefin-paraffin ratio of 1.0 and 52% CO selectivity (Fig. 6, first entry). This material has been extensively studied elsewhere, [11a, <sup>11b, 27]</sup> and is known to convert CO<sub>2</sub> via combined RWGS/FT chemistry. This combination of reactions typically produces a range of hydrocarbons, as observed, in addition to methane. Hence, iron-driven catalysts are not widely used for methanation processes. Upon incorporating nitrogen into the catalyst support, conversion and methane selectivity both increased, while CO selectivity decreased. This is likely the result of a stronger attraction between CO2, CO, and the catalyst support due to the C-N dipoles and increased Lewis basicity that arise from nitrogen doping.<sup>[28]</sup> Unlike CO<sub>2</sub> and CO, the reactive intermediates in FT synthesis do not possess such notable dipoles, and are thus less attracted to the catalyst surface - they may therefore become destabilized and readily desorb in favour of new dipole-containing adsorbents. As a result, further hydrocarbon chain lengthening is inhibited, and the FT process is more likely to terminate at methane.[29]

Doping ruthenium onto the surface of the catalyst via incipient wetness to produce Ru-Fe@NCNT further increases conversion and methane selectivity up to 71% and 91%, respectively. This places its methanation performance competitively alongside noteworthy literature examples (Table 2) while requiring 66-80%

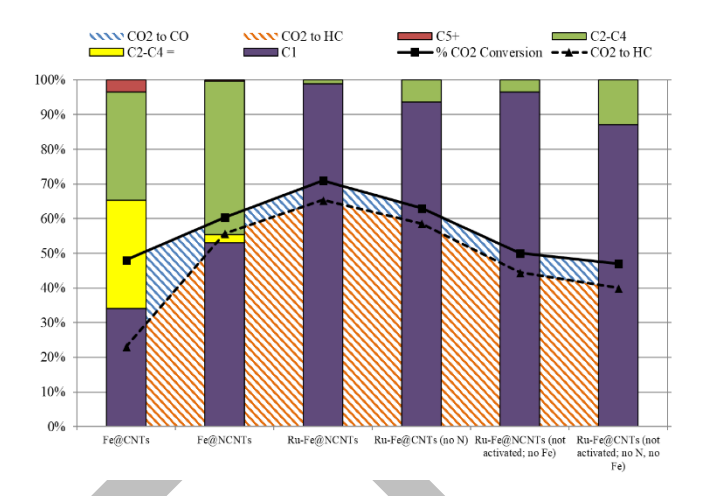


**Figure 6.** Catalytic performance of Fe@CNT, Fe@NCNT, and Ru-doped samples (both post-doped and CVD doped) at 370 °C, 15 bar, 3:1 H<sub>2</sub>:CO<sub>2</sub>, and a total flow rate of 8 sccm.

less ruthenium. Feeding the catalyst with a  $3:1~H_2:CO_2$  gas ratio likely limits the maximum possible  $CO_2$  conversion to 75% due to the overall stoichiometry of the methanation process (Equation 1), though this acceptable given the hydrogen efficiency and methane selectivity of the process (91% and 95%, respectively), and potential for  $CO_2$  recycling in an industrial application.

In order to isolate the effects of the individual components (iron, nitrogen, ruthenium) on the methanation performance of the Ru-Fe@NCNT, each dopant was systematically excluded from the catalyst during synthesis and the methanation performance was compared to Ru-Fe@NCNT (Fig. 6). Excluding nitrogen from the catalyst support resulted in a reduction in CO2 conversion by 8%, a slight decrease in methane selectivity and a slight increase in CO selectivity. Excluding iron resulted in a loss of 21% CO2 conversion, a slightly lesser decrease in methane selectivity and a slightly greater increase in CO selectivity. This confirms the trend established by the initial Fe@CNT, Fe@NCNT, and Ru-Fe@NCNT tests, suggesting that iron, nitrogen and ruthenium all contribute to CO2 conversion, while nitrogen and ruthenium are primarily responsible for shifting the product distribution towards methanation and away from CO and longer hydrocarbon production.

Excluding both nitrogen and iron from the catalyst results in the lowest conversion and methane selectivity of any ruthenium-doped samples. The observed reactivity of this sample is attributed primarily to the ruthenium catalyst, with a small effect from partially exposed iron particles that are not fully covered by the graphitic layer during synthesis, resulting in the formation of some additional CO, methane and C<sub>2+</sub> hydrocarbons. It is therefore suggested that in the full methanation process over Ru-Fe@NCNT, the iron-driven RWGS produces CO that is then rapidly consumed by both the iron via FT and the ruthenium via Sabatier chemistry, as both of these secondary reactions favour a 3:1 H<sub>2</sub>:CO<sub>2</sub> stoicheometry for methane production from CO. Thus, the addition of even a small amount of ruthenium in this

manner can serve to increase both conversion and methane selectivity by shifting the equilibrium of the iron-catalyzed RWGS even further towards products. Instances where the ruthenium agglomerates onto the surface of existing iron particles, as seen in the EDX of Ru-Fe@NCNT (Fig. 5[ii.c]), may aid in the rate of this transformation due to proximity between the two metals, allowing for more rapid CO methanation. When a 1:1 mixture of activated Fe@NCNT and unactivated Ru-Fe@NCNT was tested to limit proximity between the two active metals (Fig. 7), CO<sub>2</sub> conversion was observed to decrease by ca. 10% with a marginal decrease in methane selectivity, suggesting that the potential beneficial effect of proximity is not critical to catalytic function. It must also be stated that it is difficult to determine whether this effect is certainly due to reduced proximity between the active metals rather than the 50% reduction in overall iron and ruthenium loading as a result of the mixing the catalyst in such a manner without changing the volume of catalyst tested.

To further investigate whether the unique reactivity of Ru-Fe@NCNT arises as a result of electronic interactions between the catalytic iron and ruthenium sites versus synergistic coupling of the RWGS/FT/Sabatier reactions over distinct iron and ruthenium particles, the reactivities of post-doped Ru-Fe@NCNT and CVD-doped Ru.Fe@NCNT were compared. CVD-doped Ru,Fe@NCNT display significantly lower conversion and methane selectivity relative to Ru-Fe@NCNT (Fig. 7). C2+ selectivity increases drastically, including a surprising increase in C<sub>5+</sub> selectivity, with conversion and C<sub>5+</sub> selectivity increasing in accordance with ruthenocene loading. It was initially expected that integrating ruthenium into the catalyst during CVD synthesis would result in better interaction between the ruthenium, the iron, and the NCNT support, thereby improving methanation performance. However, despite a similar ruthenium loading between the Ru,Fe@NCNT and Ru-Fe@NCNT as determined

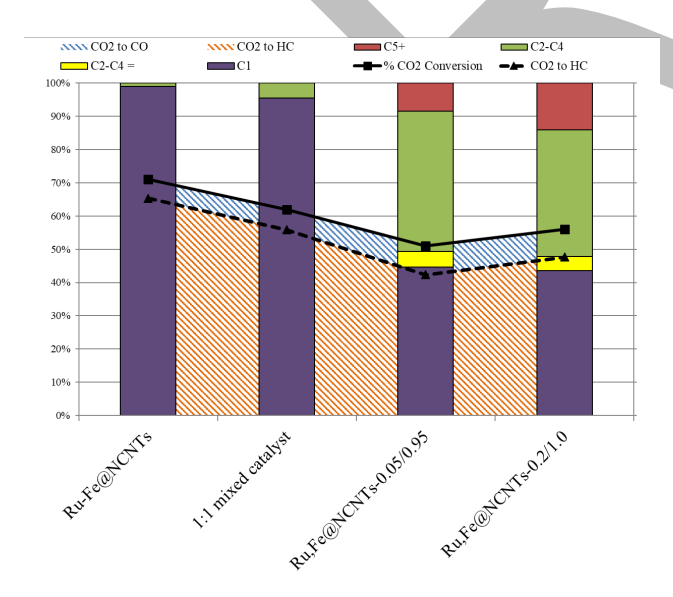


**Figure 7.** Effect of ruthenium doping via CVD versus wet impregnation, and comparison with 1:1 mixed Ru-Fe@NCNT (unactivated) and Fe@NCNT (activated).

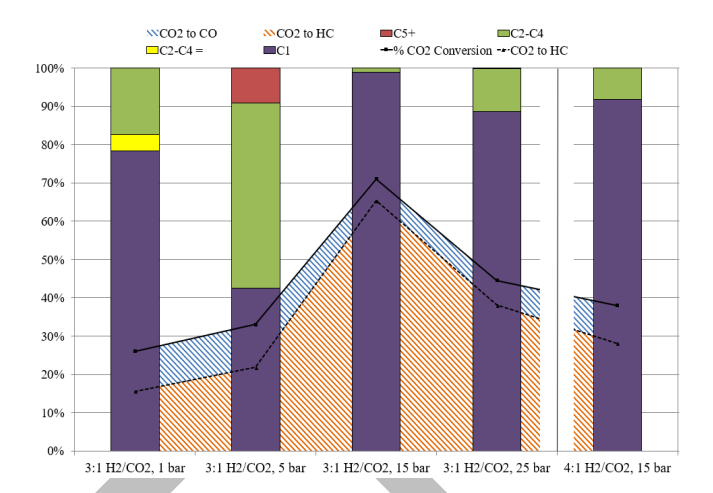


Figure 8. Effect of pressure and  $H_2/CO_2$  gas ratio on the catalytic performance of the 1 wt. % Ru-Fe@NCNT catalyst.

via XPS (SI Table 1), it appears that ruthenium plays a significantly different role in each catalyst, with distinct ruthenium particles favouring methanation in Ru-Fe@NCNT, and iron-ruthenium composite particles favouring FT chemistry in Ru,Fe@NCNT. This is in agreement with their significantly different CO<sub>2</sub> conversions and product distributions, in conjunction with differences in metal oxidation state observed via XPS (Fig. 2[ii.a-iii.b]) and XRD (Fig. 3), and the difference in ruthenium location observed via EDX (SI Fig. 4[ii.c, iii.c]). Thus, it appears that the improved methanation performance observed in post-doped Ru-Fe@NCNT occurs primarily as a result of synergistic coupling of the RWGS/FT/Sabatier reactions over distinct ruthenium and iron particles, rather than unique reactivity catalyzed by the formation of iron and ruthenium composite particles as observed in Ru,Fe@NCNT.

To further investigate the ideal reaction conditions for CO2 methanation over Ru-Fe@NCNT and confirm their operation via primarily combined RWGS/FT chemistry rather than Sabatier chemistry, the pressure and gas ratios were varied (Fig. 8). At atmospheric pressure, conversion and methane selectivity decreased significantly. At 5 bar, conversion increased marginally and selectivity shifted significantly towards C<sub>2+</sub> hydrocarbons, which would not be possible under exclusively Sabatier chemistry as C<sub>2+</sub> hydrocarbons are not possible products of the Sabatier reaction (Equation 1). 15 bar was determined to be the optimal pressure for conversion and methane selectivity, resulting in 71% CO<sub>2</sub> conversion and 91% methane selectivity with only 4% C<sub>2-4</sub> selectivity and 5% CO selectivity, as previously described. At 25 bar, conversion and methane selectivity both decreased, with selectivity shifting to favour FT again as C2+ hydrocarbons reappeared. A gas ratio of 3:1 H<sub>2</sub>:CO<sub>2</sub> was initially used as the default gas ratio, as this is well established as an ideal gas ratio for combined RWGS/FT catalysis. When a 4:1 gas ratio was tested, as is favourable for Sabatier catalysts, conversion decreased significantly to 38%, with methane selectivity decreasing to 68% and CO selectivity increasing to 26% (Fig. 8,

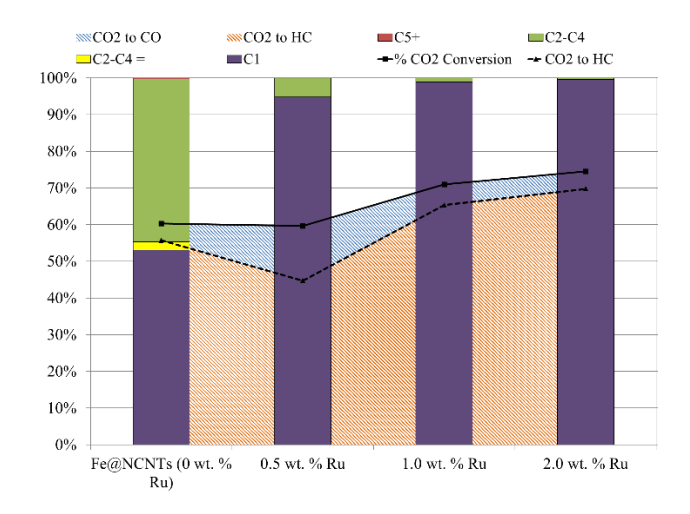
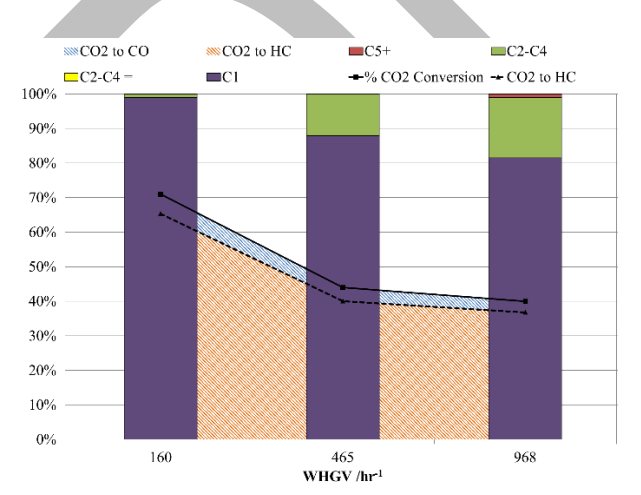


Figure 9. Effect of ruthenium loading in Ru-Fe@NCNT at 370 °C 15 bar.

final entry). This suggests that the methanation process over Ru-Fe@NCNT is still dominated by combined RWGS and FT chemistry, augmented by the addition of ruthenium rather than vice-versa.

Ruthenium loading in Ru-Fe@NCNT was also varied and 1.0 wt. % ruthenium was found to result in the most ideal balance between ruthenium savings and methanation performance (Fig. 9). 0.5 wt. % ruthenium resulted in 60% CO<sub>2</sub> conversion and 71% overall methane selectivity, with an increase in CO selectivity and decrease in C<sub>2+</sub> selectivity versus Fe@NCNT without ruthenium, as expected. 2.0 wt. % ruthenium loading resulted in 75% CO<sub>2</sub> conversion and 93% methane selectivity – a minor increase relative to 1.0 wt. % loading. This suggests that the catalyst approaches full hydrogen conversion and maximum CO<sub>2</sub> conversion at 1.0 wt. %, leading to significantly diminished returns on ruthenium loading beyond this point.



**Figure 10.** Effect of WHGV on conversion and product distribution over Ru-Fe@NCNT at 370 °C and 15 bar.

**Table 1.** Observed rate of reaction at tested WHGV values for Ru-Fe@NCNT at 370 °C and 15 bar.

WHGV [hr <sup>1</sup> ]	$R_{obs}$ [µmol g <sup>-1</sup> s <sup>-1</sup> ]	
160	2.45	
465	4.49	
968	8.53	

Weight hourly gas velocity (WHGV) was varied to assess the effect of mass transfer on the Ru-Fe@NCNT methanation process. Increasing WHGV from 160 to 968 hr<sup>-1</sup> (corresponding to an increase in total flowrate from 8 to 50 sccm) results in a significant decrease in CO2 conversion and an increase in C2+ hydrocarbons between 160 and 465 hr<sup>-1</sup>, which plateaus at ca. 40% CO<sub>2</sub> conversion and 72% methane selectivity at 968 hr<sup>-1</sup> (Fig. 10). This indicates that the process is currently limited by external mass transfer to the catalyst surface, a trend that is confirmed by the linear increase in observed rate of reaction (Table 1). This is a common phenomenon observed in powder packed bed reactors, and is a critical limitation that must be overcome through process optimization before industrial implementation. However, it has been previously shown that similar external mass transfer limitations can be overcome by supporting the catalyst on an industrial cordierite monolith support, which can be done directly during CVD synthesis - a solution that can be similarly applied to Ru-Fe@NCNT.[11c]

To further validate the chosen reaction conditions for  $CO_2$  methanation over Ru-Fe@NCNT, the equilibrium conversion of the RWGS reaction at 370 °C was calculated over a range of CO removal to account for the shift in equilibrium caused by the subsequent FT reaction. Experimental results were then compared with the equilibrium curve to determine which conditions operated closest to their maximum equilibrium performance (Fig. 11). As expected, Ru-Fe@NCNT doped with 1.0 wt. % ruthenium, operating at 15 bar and 8 sccm are shown

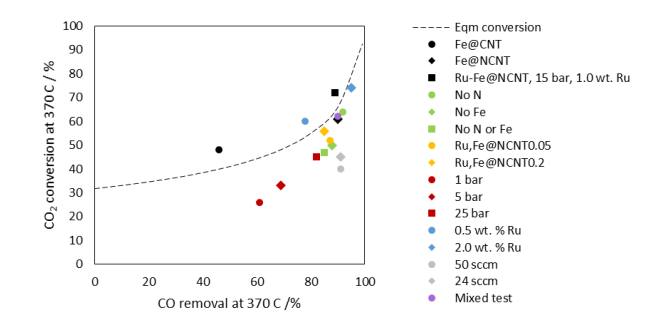


Figure 11.  $CO_2$  conversion of all tests conducted for this work plotted versus CO removal from the subsequent FT process, compared with calculated equilibrium  $CO_2$  conversion of the RWGS reaction at 370 °C from 0 to 99% CO removal.

to provide the most desirable balance of mild conditions, reduction in ruthenium loading, high CO<sub>2</sub> conversion and high methane selectivity while operating close to equilibrium. Additional ruthenium loading does not serve to significantly enhance catalyst performance, while all other tested pressures and flowrates shift performance notably further away from equilibrium.

When compared with notable methanation catalysts in recent literature (Table 2), Ru-Fe@NCNT offer several noteworthy distinctions and advantages. Modern methanation catalysts typically rely on ruthenium or nickel exclusively for their catalysis, operating via Sabatier chemistry and requiring a significant amount of the active metal at a 4:1 H<sub>2</sub>:CO<sub>2</sub> gas ratio to achieve comparable performance to Ru-Fe@NCNT. A tradeoff is also often observed between conversion and methane selectivity, as well as generally lower hydrogen conversion efficiency. Conversely, the ruthenium-augmented, iron-driven RWGS/FT/Sabatier chemistry of Ru-Fe@NCNT results in high CO<sub>2</sub> conversion and methane selectivity and nearly quantitative hydrogen conversion while operating under a 3:1 gas ratio and requiring ca. 20% of typical ruthenium loadings. While it must be noted that the quoted literature catalysts are expected to display comparable conversion and selectivity at higher pressures, it is significant that Ru-Fe@NCNT are capable of producing comparable results using much less ruthenium and alternate reaction mechanism. It is additionally noteworthy that Ru-Fe@NCNT achieve desirable methanation performance at 15 bar, while typical industrial methanation processes are cited to operate at higher pressures (ca. 10-30 bar).[30]

**Table 2.** Ru-Fe@NCNT methanation performance compared with literature and commercial catalysts.

Catalyst Temp. Pressure Feed gas X <sub>Co2</sub> selectivity X <sub>62</sub> X <sub>62+3CH</sub> liGat   Gat    [°C] [bar] [%] [%] [%] [%] [%] [wt.  5 wt. %  Co <sub>2,26</sub> Ru <sub>6,35</sub> 380 1 4.1 (H <sub>2</sub> :CO <sub>2</sub> ) 34 96 <sup>[31]</sup> 33- 33 1 1 1 1 1 1 1 1 1 1 1 1 1 1 1 1	J
5 wt. % Co <sub>RSR</sub> Russ 380 1 4:1(H <sub>2</sub> :CO <sub>2</sub> ) 34 98 <sup>(3)</sup> 33- 33 nanorods	ing
Co <sub>3.96</sub> Ru <sub>855</sub> 380 1 4.1(H <sub>2</sub> :CO <sub>2</sub> ) 34 98 <sup>(31)</sup> 33- 33 nariorods	%]
Co <sub>3.96</sub> Ru <sub>855</sub> 380 1 4.1(H <sub>2</sub> :CO <sub>2</sub> ) 34 98 <sup>(31)</sup> 33- 33 nariorods	_
nariorods 34	-
344 8 400 4 5440 7 94 0032	
2 9/ 400 4 5.4.40.7 04 02(32) 24	
Ru/Al <sub>2</sub> O <sub>3</sub> <sup>(a)</sup> (H <sub>2</sub> :CO <sub>2</sub> :N <sub>2</sub> ) 69	
5 wt. % 450 4:1:2.5 55 99 <sup>(33)</sup> 54- 54 5	
Ce <sub>0.05</sub> Ru <sub>0.05</sub> O <sub>2</sub> (H <sub>2</sub> :CO <sub>2</sub> :Ar) 55	
5 wt. % 200 1 4:1:4:1 25 91 <sup>(34)</sup> 23- 23 5	
5 Wt. % 200 44:1:4:1 25 91 23 25 Ru/Mn/Ce- (H <sub>2</sub> :CO <sub>2</sub> :N <sub>2</sub> :O <sub>2</sub> ) 25	
65/Al <sub>2</sub> O <sub>3</sub>	
GIA <sub>2</sub> O <sub>3</sub>	
Pd-Mg/SiO <sub>2</sub> 450 1 4:1:1 59 95 <sup>[35]</sup> 56- 56 -	
(H <sub>2</sub> :CO <sub>2</sub> :Ar) 59	
23 wt. % 400 1 4:1 (H <sub>2</sub> :CO <sub>2</sub> ), 81 80 <sup>(38)</sup> 65- 65 -	
Ni/CaO/Al <sub>2</sub> O <sub>3</sub> <sup>[a]</sup> 40% N <sub>2</sub> 81	
1.0 wt. % Ru- 370 15 2.97:1:0.03 71 91 95 91	
Fe@NCNT <sup>(b)</sup> (H <sub>2</sub> :CO <sub>2</sub> :Ar)	

[a] Commercial [b] this work

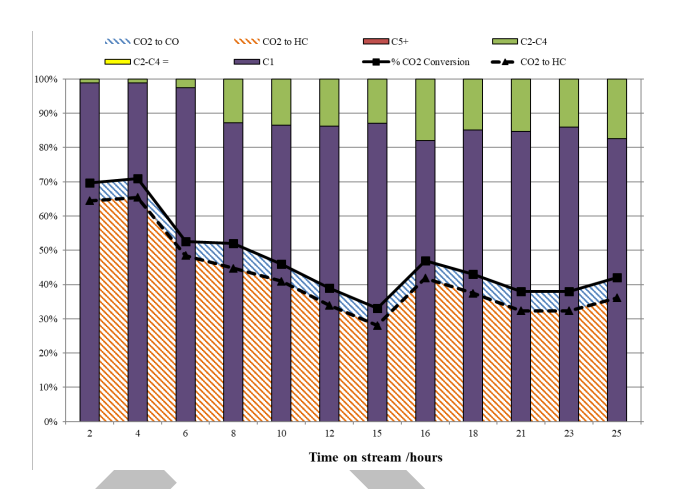


Figure 12. Equilibrium  $CO_2$  conversion of all tests conducted for this work plotted versus CO removal from the subsequent FT process, compared with calculated equilibrium  $CO_2$  conversion of the RWGS reaction at 370 °C from 0 to 99% CO removal.

Finally, Ru-Fe@NCNT were tested for 25 hours on stream to probe catalyst stability over an extended duration (Fig. 12). After 6 hours on stream, CO2 conversion decreases to ca. 50% while maintaining ca. 90% methane selectivity. After 8 hours on stream, methane selectivity is observed to decrease to ca. 70%, with CO<sub>2</sub> conversion and methane selectivity stabilizing at ca. 40% and 70% respectively after 12 hours. When viewed in the context of the increased carbon content observed in the XPS after reaction, this decrease in activity can likely be attributed in part to carbon deposition during the reaction. Nanoparticle sintering is another common cause of catalyst deactivation that is likely to contribute to the deactivation of Ru-Fe@NCNT.[37] The iron particles remain relatively stabilized against both particle migration and Ostwald ripening through their integration into the NCNT support. The ruthenium particles, however, remain susceptible to this phenomenon, which may explain the decrease in methane selectivity, as ruthenium-driven methanation deactivates more rapidly than iron-driven FT, thus resulting in a greater contribution of FT to reaction products over time.

### **Conclusions**

Ruthenium, a well-known Sabatier-driven CO<sub>2</sub> and CO methanation catalyst, was doped into Fe@NCNT, an analogue of Fe@CNT which are known to catalyse combined RWGS/FT chemistry to produce hydrocarbons from CO<sub>2</sub>. Nitrogen was additionally incorporated directly into the CNT support structure during CVD synthesis to improve the attraction of CO and CO<sub>2</sub> to the catalyst surface. Ruthenium doping was achieved via incipient wetness (Ru-Fe@NCNT) and a novel bimetallic CVD co-doping technique (Ru,Fe@NCNT) for comparison, where the doped metals existed as either distinct iron and ruthenium nanoparticles with limited interaction between them, or integrated Ru-Fe particles, respectively.

Ruthenium and nitrogen doping in Ru-Fe@NCNT were observed to shift the product distribution towards methane while exhibiting competitive CO<sub>2</sub> conversion and hydrogen efficiency, and using significantly less ruthenium than similar catalysts in the literature and industry. Conversely, Ru,Fe@NCNT exhibited poor methanation performance and produced an unexpectedly large amount of long-chain hydrocarbons. This difference in reactivity has been attributed to the different modes of ruthenium incorporation observed in the two materials, as observed via TEM, EDX, XRD and XPS analysis. The superior methanation performance of the Ru-Fe@NCNT has been attributed to synergistic coupling between several reactions over the distinct iron and ruthenium particles rather than unique chemistry arising from the formation of ruthenium-iron composites.

Different pressures, gas ratios and ruthenium loadings were applied and the effect of each dopant in the Ru-Fe@NCNT was probed to gain further information about the reaction mechanism. From these studies it is suggested that the enhanced methanation performance of Ru-Fe@NCNT at the 3:1 H<sub>2</sub>:CO<sub>2</sub> gas ratio arises from synergy between the iron-catalysed RWGS and FT reactions, and the ruthenium-catalysed Sabatier reaction. The RWGS reaction produces CO from CO2, which is rapidly converted into methane via FT and Sabatier chemistry. Nitrogen doping in the catalyst support increases conversion and encourages termination of the FT process at methane. This efficient coupling of three reactions over the same catalyst shifts the equilibrium of the initial RWGS reaction further towards products through the addition of even a small amount of ruthenium, resulting in competitive CO<sub>2</sub> conversion and superior hydrogen conversion and selectivity into methane.

Mass transfer limitations and catalyst stability must be improved in future research, and the cost of ruthenium remains significantly high compared to nickel. However, the underlying nitrogen-influenced, iron-driven FT methanation process that allows for low ruthenium loadings in Re-Fe@NCNT remains a promising platform that can be further developed to reduce the cost of CO<sub>2</sub> methanation in the future, with a logical continuation of this research based on applying nickel to the underlying Fe@NCNT rather than ruthenium. Taking this into consideration, the competitive methanation performance of Ru-Fe@NCNT combined with their desirable hydrogen efficiency, low ruthenium loading and unique position as a primarily iron-driven methanation catalyst offers an appealing alternative to standard Sabatier-based catalysts in addressing the challenge of hydrogen efficiency in CO<sub>2</sub> methanation for renewable energy storage.

#### **Experimental**

#### Materials naming convention

This article discusses several similar catalysts consisting of iron, ruthenium, and nitrogen-doped carbon nanotubes. In the primary catalyst being studied, ruthenium has been added via a conventional wet impregnation technique, resulting in ruthenium doping onto the surface of CVD-synthesized Fe@NCNT. When the ruthenium has been post-doped in

such a manner, it is separated in the sample name by a hyphen to indicate that it is added separately following the Fe@NCNT synthesis process (e.g. Ru-Fe@NCNT). For comparison, a second material has been developed in which ruthenium has been incorporated during the CVD synthesis process by dissolving ruthenocene and ferrocene together in the CVD precursor solution to promote the formation of iron-ruthenium composite particles. When the ruthenium has been CVD-doped in such a manner, it is separated in the sample name by a comma to indicate that it is incorporated during CVD synthesis, similar to the iron particles that nucleate the CNT growth (e.g. Ru,Fe@NCNT).

#### Preparation of underlying Fe@NCNT

The Fe@NCNT catalyst was prepared by dissolving 1.0 g ferrocene (FcH) in 50 mL acetonitrile (ACN) to produce a CVD precursor solution of concentration 20 mg mL $^{-1}$  FcH in ACN. 40 mL of the precursor solution was then injected at a rate of 10 mL h $^{-1}$  into a quartz tube (25 mm ID x 28 mm OD x 122 cm L), loaded in a tubular furnace at 790 °C under a flow of 50 sccm H $^{2}$  and 400 sccm Ar. After 4 hours of CVD injection, the raw catalyst was readily retrieved from within the quartz tube. A 40 mL injection synthesis typically yielded ca. 1.5 g of catalyst. To minimize error due to variance between catalyst batches, a stock of ca. 10 g was produced before beginning catalytic trials.

In this CVD process, FcH acts as the iron source for nanoparticle formation. ACN acts as the carbon and nitrogen source for the growth of the NCNT support. Flowing  $H_2$  during the CVD injection is responsible for the decomposition of the FcH in the vaporized precursor solution, resulting in deposition of iron nanoparticles along the surface of the quartz tube. [38] These nanoparticles nucleate the growth of Fe@NCNT, utilizing the vaporized ACN as a source of carbon and nitrogen. Flowing argon acts as an inert carrier gas for the vaporized precursor solution, and ensures that no oxygen is present in the CVD reactor. In order to produce Fe@CNT (no nitrogen doped into the nanotube lattice), the precursor solvent was replaced by toluene while all other conditions remained unchanged.

#### Preparation of post-doped Ru-Fe@CNT and Ru-Fe@NCNT

A wet impregnation technique was used to dope ruthenium nanoparticles onto the surface of Fe@CNT and Fe@NCNT. In order to achieve 1.0 wt. % ruthenium doping, 11 mg RuCl<sub>3</sub> (min. 47.7% Ru, Alfa Aesar) and 0.5 g catalyst were stirred in 15 mL methanol at room temperature for 24 hours. Though the methanol had typically evaporated after 24 hours, the catalyst was additionally heated for 1.5 hours at 100 °C to dry. This produced sufficient Ru-Fe@CNT or Ru-Fe@NCNT material to conduct one methanation test. To minimize variance between catalyst batches, this process was scaled up to dope 1.5 g catalyst with 33 mg RuCl<sub>3</sub> in 45 mL methanol, which produced enough catalyst for 3 methanation tests.

#### Preparation of CVD-doped Ru,Fe@NCNT

To dope ruthenium onto the Fe@NCNT directly during the CVD synthesis process, ruthenocene was dissolved in the ACN precursor solution in conjunction with ferrocene, while all other conditions remained unchanged. Two ratios of ruthenocene to ferrocene were tested, producing samples labeled as Ru,Fe@NCNT-X/Y, where X and Y represent the masses of ruthenocene and ferrocene dissolved in 50 mL ACN to produce the precursor solution in grams, respectively. The ruthenocene/ferrocene loadings used were 0.05/0.95 and 0.20/1.0, to probe the effect of increasing ruthenium concentrations at similar levels to the post-doped catalysts. Ruthenocene was chosen as the ruthenium source, as it was likely to decompose in  $\rm H_2$  flow via a similar mechanism as the ferrocene used during synthesis.

#### Catalyst activation

Catalysts were activated via thermal oxidation in air to expose the catalytic metal sites, which have been previously reported to be concealed by a graphitic carbon layer during synthesis, preventing them from engaging in catalysis unless this graphitic layer is removed. [11a] In the post-doped Ru-Fe@NCNT and Ru-Fe@CNT, this activation step served primarily to expose the catalytic iron nanoparticles embedded in the nanotube lattice, as the post-doped ruthenium particles did not require exposing. In the CVD-doped Ru, Fe@NCNT, this step served to expose both iron and ruthenium.

For any NCNT-based catalysts, 0.5 g catalyst was loaded into a stainless steel calcination tube (0.5 inch OD x 0.451 ID x 6 inch L), which was plugged with quartz wool at one end to allow for air flow. The tube was then heated in a muffle oven at 400 °C for 1 hour under a static air atmosphere, with a heating ramp rate of 10 °C min<sup>-1</sup>. For any CNT-based catalysts, the same process was repeated, though the catalysts were instead heated to 570 °C for 40 min, as pure CNTs without nitrogen doped into the surface are known to be more thermally stable than NCNTs, which degrade faster when heated due to lattice defects introduced during nitrogen doping. [39]

#### CO<sub>2</sub> methanation testing

Methanation tests were carried out by loading 0.4 g (3.1 cm³) of the desired catalyst into a stainless steel reaction tube (0.5 inch OD x 0.451 inch ID x 6 inch L), which was plugged with quartz wool at both ends to ensure that the catalyst powder rested securely in the middle of the tube. The reaction tube was then placed in a tubular furnace and heated to 400 °C for 3 hours under a flow of 50 sccm H<sub>2</sub> at atmospheric pressure to reduce the catalytic metal sites and saturate the catalyst support with hydrogen. [40] This allows for the formation of iron carbide species that catalyze the FT process to form hydrocarbons from CO, following the initial RWGS step. [8a, 41] After reaction, these carbide species are not maintained and the particles return to their initial iron oxide state.

To begin the methanation process, the temperature was lowered to 370 °C and the pressure gradually raised to the desired reaction pressure (typically 15 bar), while maintaining the desired reaction gas ratio (typically 3:1 H<sub>2</sub>:CO<sub>2</sub>). A high overall flow rate (180 sccm) was employed during this step to facilitate pressurization of the reactor. When the desired pressure had been achieved, the flow rate was lowered to the desired reaction flowrate (typically 8 sccm). The reactor was left for 2 hours to equilibrate following pressurization, after which samples were taken hourly for 3 hours via a gas syringe and analyzed via GC-MS. Stability testing was conducted over 1 week, where the catalyst was left at the reaction temperature and atmospheric pressure under argon overnight.

A 1% Ar in  $H_2$  gas mixture was used as the  $H_2$  source. This allowed for any change in volume due to the reaction to be accounted for by using the Ar as an internal standard during GC-MS analysis. A calibration curve was plotted using 100%, 50% and 33% Ar/ $H_2$  mix in CO and CO<sub>2</sub> to ensure an accurate response from the internal standard. Carbon balances were calculated for all samples and were found to range from 90-110% in all cases.

#### Dopant exclusion

To assess the effect of each dopant in the Ru-Fe@NCNT (as seen in Fig. 6), each dopant was systematically excluded during catalyst synthesis. To

exclude ruthenium, the wet impregnation process was not performed. To exclude nitrogen, Fe@CNT were used as the underlying catalyst rather than Fe@NCNT. To exclude iron, the thermal activation step was not performed, thus leaving the iron nanoparticles obscured beneath their graphitic layer and preventing them from participating in catalysis.

#### Materials characterization

Raman analysis was conducted using a Renishaw inVia system and a 532 nm laser at 0.1% power for an exposure time of 400 seconds to avoid decomposing the sample during analysis. SEM analysis was conducted using a JEOL SEM6480LV in secondary electron imaging mode at an accelerating voltage of 10 kV. FESEM analysis was conducted using a JEOL FESEM6301F at an accelerating voltage of 5 kV. TEM analysis was conducted using aa JEOL JSM-2100PLUS at an accelerating voltage of 200 kV. XPS analysis was conducted using a Kratos Axis Ultra-DLD system through the Newcastle University NEXUS XPS facilities and a Thermo Fisher Scientific K-alpha+ spectrometer through the Cardiff University XPS analysis facilities. Samples were analysed using a microfocused monochromatic Al X-ray source (72 W) over an area of approximately 400 microns. Data was recorded at pass energies of 150 eV for survey scans and 40 eV for high resolution scan with 1 eV and 0.1 eV step sizes respectively. Charge neutralisation of the sample was achieved using a combination of both low energy electrons and argon ions.

Data analysis was performed in CasaXPS using a Shirley type background and Scofield cross sections, with an energy dependence of -0.6. XRD was conducted using a Bruker D8 Advance with Vantec Detector with Cu K- $\alpha_1$  radiation. Samples were scanned in flat plate mode at 2 $\theta$  values of 20-80° with a scan rate of 0.27-0.18° min<sup>-1</sup> (4-6 hours per sample).

### **Acknowledgements**

The authors would like to acknowledge the following entities for their critical contributions to this work: the Microscopy and Analysis Suite (MAS) at the University of Bath for their assistance and expertise in characterising the described materials via Raman, SEM, FESEM, TEM and EDX. The National EPSRC XPS Users' Service (NEXUS) at Newcastle University for their assistance and expertise in characterising the underling Fe@NCNT materials via XPS. Dr David Morgan and the XP Spectrometry Suite at Cardiff University for their assistance and expertise in characterising the ruthenium-doped samples via XPS. Dr Pawel Plucinski of the Department of Chemical Engineering at the University of Bath for his assistance and expertise in reaction kinetics and thermodynamics. The UK Engineering and Physical Sciences Research Council (EPSRC) for their generous funding of this research.

**Keywords:** methanation • CO2 • iron • carbon nanotube • catalysis

- [1] aT. A. Le, M. S. Kim, S. H. Lee, T. W. Kim, E. D. Park, *Catalysis Today* **2017**, *293-294*, 89-96; bS. Rönsch, J. Schneider, S. Matthischke, M. Schlüter, M. Götz, J. Lefebvre, P. Prabhakaran, S. Bajohr, *Fuel* **2016**, *166*, 276-296.
- [2] aE. V. Kondratenko, G. Mul, J. Baltrusaitis, G. O. Larrazabal, J. Perez-Ramirez, *Energy & Environmental Science* **2013**, 6,

- 3112-3135; bM. Bui, C. S. Adjiman, A. Bardow, E. J. Anthony, A. Boston, S. Brown, P. S. Fennell, S. Fuss, A. Galindo, L. A. Hackett, J. P. Hallett, H. J. Herzog, G. Jackson, J. Kemper, S. Krevor, G. C. Maitland, M. Matuszewski, I. S. Metcalfe, C. Petit, G. Puxty, J. Reimer, D. M. Reiner, E. S. Rubin, S. A. Scott, N. Shah, B. Smit, J. P. M. Trusler, P. Webley, J. Wilcox, N. Mac Dowell, *Energy & Environmental Science* 2018; cK. Müller, M. Städter, F. Rachow, D. Hoffmannbeck, D. Schmeißer, *Environmental Earth Sciences* 2013, 70, 3771-3778; dS. H. Jensen, C. Graves, M. Mogensen, C. Wendel, R. Braun, G. Hughes, Z. Gao, S. A. Barnett, *Energy & Environmental Science* 2015, 8, 2471-2479.
- [3] aM. A. Vannice, Journal of Catalysis 1975, 37, 462-473; bJ. Kirchner, J. K. Anolleck, H. Lösch, S. Kureti, Applied Catalysis B: Environmental 2018, 223, 47-59; cJ. Gao, Q. Liu, F. Gu, B. Liu, Z. Zhong, F. Su, RSC Advances 2015, 5, 22759-22776; dl. Kuznecova, J. Gusca, Energy Procedia 2017, 128, 255-260.
- [4] M. Younas, L. Loong Kong, M. J. K. Bashir, H. Nadeem, A. Shehzad, S. Sethupathi, *Energy & Fuels* **2016**, *30*, 8815-8831.
- [5] C. Liu, T. R. Cundari, A. K. Wilson, *The Journal of Physical Chemistry C* **2012**, *116*, 5681-5688.
- [6] B. Miao, S. S. K. Ma, X. Wang, H. Su, S. H. Chan, *Catalysis Science & Technology* **2016**, *6*, 4048-4058.
- [7] K. Stangeland, D. Kalai, H. Li, Z. Yu, *Energy Procedia* **2017**, *105*. 2022-2027.
- [8] aG. Prieto, *ChemSusChem* **2017**, *10*, 1056-1070; bL. M. Chew, P. Kangvansura, H. Ruland, H. J. Schulte, C. Somsen, W. Xia, G. Eggeler, A. Worayingyong, M. Muhler, *Applied Catalysis A: General* **2014**, *482*, 163-170; cP. Kaiser, R. B. Unde, C. Kern, A. Jess, *Chemie Ingenieur Technik* **2013**, *85*, 489-499.
- [9] R. E. Owen, D. Mattia, P. Plucinski, M. D. Jones, *ChemPhysChem* **2017**, *18*, 3211-3218.
- [10] aR. W. Dorner, D. R. Hardy, F. W. Williams, B. H. Davis, H. D. Willauer, *Energy & Fuels* **2009**, 23, 4190-4195; bP. Kangvansura, L. M. Chew, C. Kongmark, P. Santawaja, H. Ruland, W. Xia, H. Schulz, A. Worayingyong, M. Muhler, *Engineering* **2017**, 3, 385-392; cY. A. Daza, J. N. Kuhn, *RSC Advances* **2016**, 6, 49675-49691; dJ. Wei, Q. Ge, R. Yao, Z. Wen, C. Fang, L. Guo, H. Xu, J. Sun, *Nature Communications* **2017**, 8, 15174.
- [11] aJ. P. O'Byrne, R. E. Owen, D. R. Minett, S. I. Pascu, P. K. Plucinski, M. D. Jones, D. Mattia, *Catalysis Science & Technology* **2013**, *3*, 1202-1207; bD. Mattia, M. D. Jones, J. P. O'Byrne, O. G. Griffiths, R. E. Owen, E. Sackville, M. McManus, P. Plucinski, *ChemSusChem* **2015**, *8*, 4064-4072; cD. R. Minett, J. P. O'Byrne, S. I. Pascu, P. K. Plucinski, R. E. Owen, M. D. Jones, D. Mattia, *Catalysis Science & Technology* **2014**, *4*, 3351-3358.
- [12] M. S. Dresselhaus, A. Jorio, A. G. Souza Filho, R. Saito, *Philosophical Transactions of the Royal Society A: Mathematical, Physical and Engineering Sciences* **2010**, 368, 5355.
- [13] T. Sharifi, F. Nitze, H. R. Barzegar, C.-W. Tai, M. Mazurkiewicz, A. Malolepszy, L. Stobinski, T. Wågberg, *Carbon* **2012**, *50*, 3535-3541.
- [14] W. J. Lee, U. N. Maiti, J. M. Lee, J. Lim, T. H. Han, S. O. Kim, *Chem Commun (Camb)* **2014**, *50*, 6818-6830.
- [15] R. A. DiLeo, B. J. Landi, R. P. Raffaelle, *Journal of Applied Physics* 2007, 101, 064307.

- [16] aS. Maldonado, S. Morin, K. J. Stevenson, *Carbon* **2006**, *44*, 1429-1437; bS. van Dommele, A. Romero-Izquirdo, R. Brydson, K. P. de Jong, J. H. Bitter, *Carbon* **2008**, *46*, 138-148; cH. Xiong, M. A. Motchelaho, M. Moyo, L. L. Jewell, N. J. Coville, *Applied Catalysis A: General* **2014**, *482*, 377-386.
- [17] L. Yin-Chih, H. Jhen-Yong, Y. Chia-Nan, T. Shi-Yuan, T. Mean-Jue, S. Hung-Wei, C. Chia-Hao, L. Minn-Tsong, *Japanese Journal of Applied Physics* **2015**, *54*, 033002.
- [18] aT. Yamashita, P. Hayes, *Applied Surface Science* **2008**, 254, 2441-2449; bM. C. Biesinger, B. P. Payne, A. P. Grosvenor, L. W. M. Lau, A. R. Gerson, R. S. C. Smart, *Applied Surface Science* **2011**, 257, 2717-2730.
- [19] aD. J. Morgan, Surface and Interface Analysis 2015, 47, 1072-1079; bR. Bavand, A. Yelon, E. Sacher, Applied Surface Science 2015, 355, 279-289.
- [20] D. Chen, Q. Tang, X. Li, X. Zhou, J. Zang, W.-q. Xue, J.-y. Xiang, C.-q. Guo, *International Journal of Nanomedicine* **2012**, 7, 4973-4982.
- [21] A. Azam, A. S. Ahmed, M. Oves, M. S. Khan, S. S. Habib,A. Memic, *International Journal of Nanomedicine* 2012, 7, 6003-6009
- [22] N. Abatzoglou, B. Legras, International Journal of Environmental Pollution and Remediation (IJEPR) 2015, 3, 9-15. [23] aJ. Z. Bloh, R. Dillert, D. W. Bahnemann, Physical Chemistry Chemical Physics 2014, 16, 5833-5845; bL. S. Panchakarla, A. Govindaraj, Bulletin of Materials Science 2007, 30, 23-29; cJ. Liu, P. Bai, X. S. Zhao, Physical Chemistry Chemical Physics 2011, 13, 3758-3763.
- [24] T. H. Pham, Y. Qi, J. Yang, X. Duan, G. Qian, X. Zhou, D. Chen, W. Yuan, *ACS Catalysis* **2015**, *5*, 2203-2208.
- [25] R. Yadav, P. Dobal, T. Shripathi, R. Katiyar, O. Srivastava, *Nanoscale Research Letters* **2008**, *4*, 197.
- [26] C. T. Wirth, B. C. Bayer, A. D. Gamalski, S. Esconjauregui, R. S. Weatherup, C. Ducati, C. Baehtz, J. Robertson, S. Hofmann, *Chemistry of Materials* **2012**, *24*, 4633-4640.
- [27] L. Torrente-Murciano, D. Mattia, M. D. Jones, P. K. Plucinski, *Journal of CO2 Utilization* **2014**, *6*, 34-39.
- [28] aH. Kiuchi, R. Shibuya, T. Kondo, J. Nakamura, H. Niwa, J. Miyawaki, M. Kawai, M. Oshima, Y. Harada, *Nanoscale Research Letters* **2016**, *11*, 127; bJ. Lu, L. Yang, B. Xu, Q. Wu, D. Zhang, S. Yuan, Y. Zhai, X. Wang, Y. Fan, Z. Hu, *ACS Catalysis* **2014**, *4*, 613-621.
- [29] J. Gaube, H. F. Klein, *Journal of Molecular Catalysis A: Chemical* **2008**, 283, 60-68.
- [30] aT. Schaaf, J. Grünig, M. R. Schuster, T. Rothenfluh, A. Orth, *Energy, Sustainability and Society* **2014**, *4*, 2; bZ. He, X. Wang, S. Gao, T. Xiao, *Applied Petrochemical Research* **2015**, *5*, 413-417; cK. Ghaib, in *Das Power-to-Methane-Konzept*, Springer, **2017**, pp. 29-32.
- [31] Y. Zhu, S. Zhang, Y. Ye, X. Zhang, L. Wang, W. Zhu, F. Cheng, F. Tao, *ACS Catalysis* **2012**, *2*, 2403-2408.
- [32] aG. Garbarino, D. Bellotti, P. Riani, L. Magistri, G. Busca, *International Journal of Hydrogen Energy* **2015**, *40*, 9171-9182; bP. Frontera, A. Macario, M. Ferraro, P. Antonucci, *Catalysts* **2017**, *7*, 59.
- [33] S. Sharma, Z. Hu, P. Zhang, E. W. McFarland, H. Metiu, *Journal of Catalysis* **2011**, *278*, 297-309.

[34] S. Toemen, W. A. W. A. Bakar, R. Ali, *Journal of the Taiwan Institute of Chemical Engineers* **2014**, *45*, 2370-2378.

[35] J.-N. Park, E. W. McFarland, *Journal of Catalysis* **2009**, 266, 92-97.

[36] B. Mutz, H. W. P. Carvalho, S. Mangold, W. Kleist, J.-D. Grunwaldt, *Journal of Catalysis* **2015**, 327, 48-53.

[37] T. W. Hansen, A. T. DeLaRiva, S. R. Challa, A. K. Datye, *Accounts of Chemical Research* **2013**, *46*, 1720-1730.

[38] K. Kuwana, K. Saito, *Proceedings of the Combustion Institute* **2007**, *31*, 1857-1864.

[39] aE. N. Nxumalo, N. J. Coville, *Materials* **2010**, *3*, 2141-2171; bX. Ma, E. G. Wang, *Applied Physics Letters* **2001**, *78*, 978-980; cR. Kurt, A. Karimi, *ChemPhysChem* **2001**, *2*, 388-392.

[40] S. T. Srinivas, P. K. Rao, Journal of Catalysis 1994, 148, 470-477.

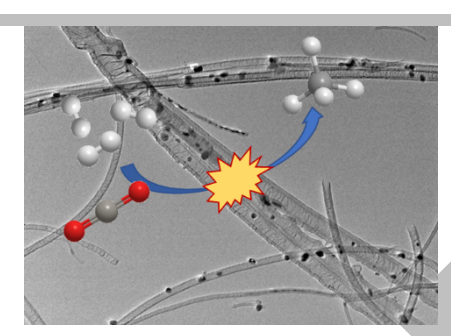
[41] aH. J. Schulte, B. Graf, W. Xia, M. Muhler, *ChemCatChem* **2012**, *4*, 350-355; bK. Xu, B. Sun, J. Lin, W. Wen, Y. Pei, S. Yan, M. Qiao, X. Zhang, B. Zong, *Nature Communications* **2014**, *5*, 5783; cA. N. Conejo, R. S. Estrada, *steel research international* **2007**, *78*, 3-9; dV. V. Ordomsky, B. Legras, K. Cheng, S. Paul, A. Y. Khodakov, *Catalysis Science & Technology* **2015**, *5*, 1433-1437.



## **Entry for the Table of Contents**

# **FULL PAPER**

An iron-driven methanation catalyst provides an alternate mechanism and improved hydrogen and ruthenium efficiency for CO<sub>2</sub> methanation.



David L. Williamson, Matthew D. Jones\* and Davide Mattia\*

Page No. – Page No.

Highly selective, iron-driven CO<sub>2</sub> methanation

